Mechanism of continuous intergranular phase formation in $Sm(Fe,Ti,V)_{12}$-based sintered magnets by post-sinter annealing

J.S. Zhang, Xin Tang*, T. Ohkubo, K. Hono, H. Sepehri-Amin

National Institute for Materials Science, Tsukuba 305-0047, Japan

Abstract:

We investigated the post-sinter annealing process in $Sm_8Fe_{77}Ti_5V_8Al_2$ (Cu-free) and $Sm_8Fe_{76.5}Ti_5V_8Al_2Cu_{0.5}$ (Cu-doped) magnets to explore the possibility of achieving high coercivity in the $SmFe_{12}$-based sintered magnets. We found that optimal annealing of the Cu-doped magnet resulted in a significant increase in coercivity from 0.9 T to 1.5 T, the highest coercivity ever reported for a $SmFe_{12}$-based magnet. This represents a 67% improvement, compared to a 13% increase in the Cu-free system. Combined with a larger remanence due to the minimization of the Fe_2Ti phase, a good combination of extrinsic magnetic properties, a remanence of 0.71 T, a coercivity of 1.5 T and the maximum energy product of 84 kJ/m^3 were obtained. The optimum post-sinter annealing temperature was found to be 1100 ºC, where a continuous Sm-rich intergranular phase is formed due to the phase equilibrium with the $ThMn_{12}$-type $Sm(Fe,V,Ti)_{12}$ phase. The underlying mechanisms for the coercivity enhancement revealed by this work provide insights for the development of high-performance $SmFe_{12}$-based magnets for practical applications.

Keywords: $SmFe_{12}$; Anisotropic sintered magnet; Cu-doping; Post-sinter annealing; High coercivity

*Corresponding author: Tang.Xin@nims.go.jp

1. Introduction

In recent years, the study of Fe-rich $SmFe_{12}$-based (1:12) compounds has been revived due to their excellent intrinsic magnetic properties, minimal rare earth content, and the potential as an alternative to Nd-Fe-B type magnets [1-8]. It is well-known that the $SmFe_{12}$ binary phase is thermodynamically unstable in the bulk form [9]. Therefore,

additives such as Ti, V, Mo, Al, Ga, Cr, Mn, W, and Si are essential to stabilize the $ThMn_{12}$-type structure in bulk materials, but at the expense of the saturation magnetization, $\mu_0 M_s$, of the magnets [10-16]. Among them, Ti is efficient in achieving a stable $ThMn_{12}$-type crystal structure due to its minimum doping amount [17-19], while V is crucial to realize large coercivity in bulk by forming Sm-rich intergranular phases [20]. Recent developments in anisotropic sintered $SmFe_{12}$-based magnets have demonstrated a coercivity of 0.8 - 1.0 T, which is attributed to the formation of a Sm-rich intergranular phase due to the equilibrium between the V-containing main phase and the Sm-rich phase [21-23]. A further increase in coercivity to 1.4 T has been achieved by microalloying with Cu in Ti-rich $Sm_8Fe_{73.5}Ti_8V_8Al_2Cu_{0.5}$ composition, which improves the wettability of the Sm-rich intergranular phase (IGP) [24]. A similar effect of Cu on the microstructure and coercivity has also been reported in $SmFe_{12}$ thin film infiltrated by Cu [25] and $Sm(Fe,V)_{12}$-based nanocrystalline alloys with Cu addition [26, 27]. Therefore, achieving continuous intergranular phase is crucial for enhancing coercivity. However, the most important mechanism behind the formation of continuous intergranular phases through Cu addition remains elusive, particularly with respect to when and where this formation occurs. Understanding this process is essential for controlling the microstructure to achieve high coercivity in $SmFe_{12}$-based sintered magnets. In addition, the low remanent magnetization of 0.6 T in the fabricated magnets due to the presence of excessive stabilizing elements remains a major bottleneck for practical applications. Although a remanent magnetization of 0.79 T was previously achieved in Ti-lean $Sm_8Fe_{76.5}Ti_5V_8Al_2Ga_{0.5}$, it came at the cost of low coercivity (0.6 T) due to strong exchange coupling between matrix phase [23]. In this work, we demonstrate that adding Cu to a Ti-lean composition significantly enhances coercivity while minimizing the loss of remanence.

In Nd-Fe-B-based sintered magnets, the formation of intergranular phase (IGP) is induced by a low-temperature (~ 480-750 ºC) post-sinter annealing process, in which the low-melting-point Nd-Cu eutectic infiltrates from triple junctions into the grain boundaries via the capillary effect [28-33]. This results in the formation of a continuous

IGP that envelops the $Nd_2Fe_{14}B$ grains, weakening the intergranular exchange coupling and thereby increasing the coercivity without reducing the remanence. This raises the question of whether such an approach can be applied to the $SmFe_{12}$-based system. Although coercivity enhancement by Cu doping has been reported in previous work on $SmFe_{12}$-based sintered magnets, a clear understanding of the role of Cu in microstructure and coercivity during the annealing process has not been disclosed. Therefore, comprehensive studies on the influence of Cu and the annealing process on microstructure and coercivity are needed for further improvements. To the best of our knowledge, the effects of post-sinter annealing have not yet been studied in $SmFe_{12}$-based sintered magnets. Our findings provide valuable guidance for microstructure engineering in this emerging class of hard magnetic materials.

In this work, we have systematically compared the microstructure evolution during the annealing process for Cu-doped and Cu-free $Sm(Fe,Ti,V,Al)_{12}$-based sintered magnets. This study reveals the role of Cu in suppressing the unwanted $SmFe_2$ phase and shows that the formation of continuous IGP in Cu-doped magnets results from the equilibrium between the $SmFe_{12}$-based main phase and the Sm-rich phase at 1100°C, which is different from the mechanism proposed for Nd-Fe-B-based sintered magnets. In addition, based on our previous work [23], we focused on Ti-lean compositions to minimize the Fe_2Ti phase for higher remanence. Our efforts have resulted in a notable enhancement in coercivity from 0.6 T [23] to 1.5 T in the present Cu-doped Ti-lean composition, while simultaneously improving remanence from 0.6 T [24] to 0.71 T.

2. Experimental

The magnets investigated in this study with nominal compositions of $Sm_8Fe_{77}Ti_5V_8Al_2$ (denoted as Cu-free) and $Sm_8Fe_{76.5}Ti_5V_8Al_2Cu_{0.5}$ (denoted as Cu-doped), respectively were produced by conventional powder metallurgy method, including induction melting, strip-casting followed by homogenizing annealing at 1100 ℃ for 12 hours to eliminate the undesired secondary phases, hydrogen decrepitation (HD), jet-milling by N_2 gas under a pressure of 0.8-1.0 MPa for obtaining

powder with the mean particle sizes around 3 μm, green compacting after orientating under a magnetic field of 5 T and liquid phase sintering at 1100 ℃ for 1.5 hours in Ar atmosphere. The selected two Ti-lean compositions is aiming to achieve high remanence by minimizing the Fe_2Ti phase and Cu addition is expected to facilitate the formation of Sm-rich intergranular phase as reported in our previous publications [23, 24]. The optimized Cu content of 0.5 at.% was determined based on systematic investigation of sintered $Sm_8Fe_{77-x}Ti_5V_8Al_2Cu_x$ with x = 0, 0.5, 1.0, and 1.5 (see Fig. S1). Increasing Cu content above 0.5 at.% resulted in the formation of undesired α-Fe phase. The as-sintered magnets then underwent the post-sinter heat-treatment at 500-1100 ℃ for 0 - 3 hours in Ar atmosphere to study the effect of post-sinter annealing (PSA) on the microstructure and magnetic properties. To minimize Sm loss during annealing, Sm metal was put into the annealing chamber to create a Sm-rich atmosphere. Additionally, the surfaces of all annealed samples were carefully polished prior to characterization.

The hard magnetic properties of the sintered magnets were evaluated by using a vibrating sample magnetometer (VSM) equipped in the physical property measurement system (Quantum Design DynaCool-14T). The constituent phases in the samples were characterized by Rigaku MiniFlex X-ray diffractometer with λ= 2.29 Å (Cr-Kα radiation). The general microstructures were characterized by scanning electron microscope (SEM, Carl Zeiss Cross-Beam 1540EsB) after focused ion beam (FIB) polishing. Detailed microstructural investigations were performed on a Titan G2 80-200 transmission electron microscope (TEM) with a probe aberration corrector. Magnetic domain observation was performed in the Lorentz-Fresnel mode in the TEM. All specimens for TEM observation were prepared using lift-out technique in a FEI Helios G4-UX FIB system.

3. Results

3.1. Magnetic properties

Fig. 1a and 1c shows coercivity ($\mu_0 H_c$) and the change ($\Delta\mu_0 H_c$) in coercivity as a

function of post-sinter annealing temperature for Cu-doped and Cu-free magnets. In the case of Cu-doped sample, a significant increase in coercivity from 0.9 T to 1.5 T was observed after optimal annealing at 1100°C for 1.5 hours. The coercivity obtained is the highest reported so far for the anisotropic $SmFe_{12}$-based sintered magnets. In contrast, the improvement of the coercivity on Cu-free magnets upon post-sinter annealing is very limited even at the optimal annealing temperature, increasing only from 0.93 T to 1.05 T. Unexpectedly, a decrease of the coercivity was observed at the annealing temperature lower than 800°C. The hysteresis loops of the magnets annealed at various temperatures are shown in Supplementary Figure S2. The selected the hysteresis loops for optimally annealed magnets are shown in Fig. 1b and 1d. The as-sintered Cu-free and Cu-doped magnets exhibit similar values of coercivity $\mu_0 H_c$, 0.93 T and 0.9 T, respectively. The remanent magnetization ($\mu_0 M_r$) and maximum energy product ($(BH)_{max}$) were measured for the post-sinter annealed samples (at 1100°C for 1.5 hours) to be 0.69 T and 77 kJ/m³ for the Cu-free sample, and 0.71 T and 84 kJ/m³ for the Cu-doped sample, respectively. Compared to previously reported $Sm_8Fe_{76.5}Ti_5V_8Al_2Ga_{0.5}$ sintered magnets, the Cu-doped magnets in this study exhibit the best combination of remanence and coercivity [23, 24]. Note that the optimal annealing temperature for $SmFe_{12}$-based magnet is 1100 °C, which is much higher than that (~480 - 750 ºC) for Nd-Fe-B sintered magnet [31]. Further increase of the annealing temperature results in a sudden drop of the coercivity as shown in Figure S2. The kink observed in the hysteresis loop suggests the formation of an inhomogeneous microstructure likely caused by overheating. The question is: what microstructural features contribute to the coercivity enhancement in $SmFe_{12}$-based magnets, which may differ from those in Nd-Fe-B magnets? To answer this question, we conducted detailed microstructural investigations on the samples.

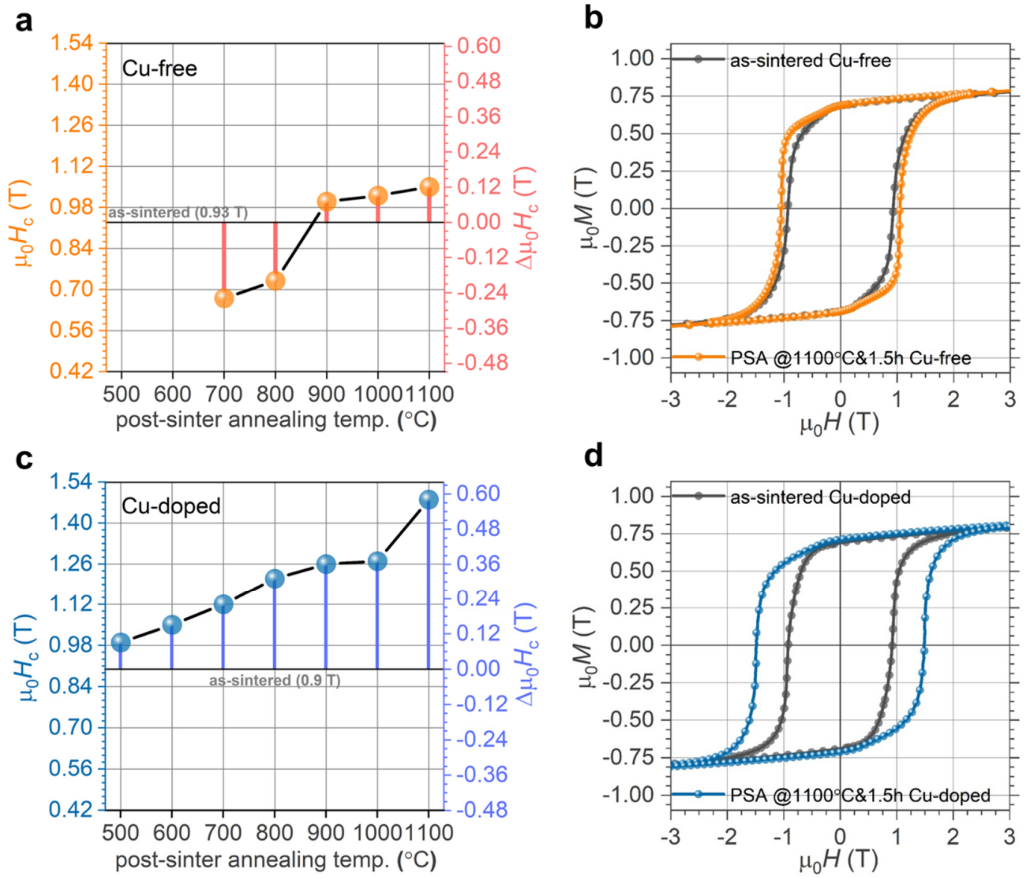

Fig. 1. a), c) Post-sinter annealing temperature dependent of coercivity $\mu_0 H_c$ and coercivity increment, $\Delta\mu_0 H_c$, for $Sm_8Fe_{77}Ti_5V_8Al_2$ (Cu-free) and $Sm_8Fe_{76.5}Ti_5V_8Al_2Cu_{0.5}$ (Cu-doped) sintered magnets, the black horizontal line denotes the coercivity of as-sintered magnet. b), d) Hysteresis loops of Cu-free and Cu-doped magnets of as-sintered and post-sinter annealed at 1100 °C for 1.5 h.

3.2. Phase constituents and Overall microstructure

Fig. 2 shows the XRD profiles of both Cu-free and Cu-doped samples in the as-sintered state and after post-sinter annealing at different temperatures for a fixed period of 1.5 hours. To improve the resolution of the minor secondary phases, the annealed samples were pulverized into powders before the XRD measurements. The XRD patterns show that all samples contain the primary $ThMn_{12}$-type phase (hereafter denoted as 1:12 phase), along with metallic Sm and SmO phases. In the Cu-free samples, the $SmFe_2$ phase with $MgCu_2$ crystal structure was detected across all the annealing

conditions. Under the low temperature annealing condition, we observe the increase in the number density of the $SmFe_2$ phase as shown in Figure S4 and the coercivity decrease observed after low-temperature annealing in the Cu-free sample requires further investigation. In contrast, Fig. 2b suggests that the formation of $SmFe_2$ phase was effectively suppressed by Cu addition.

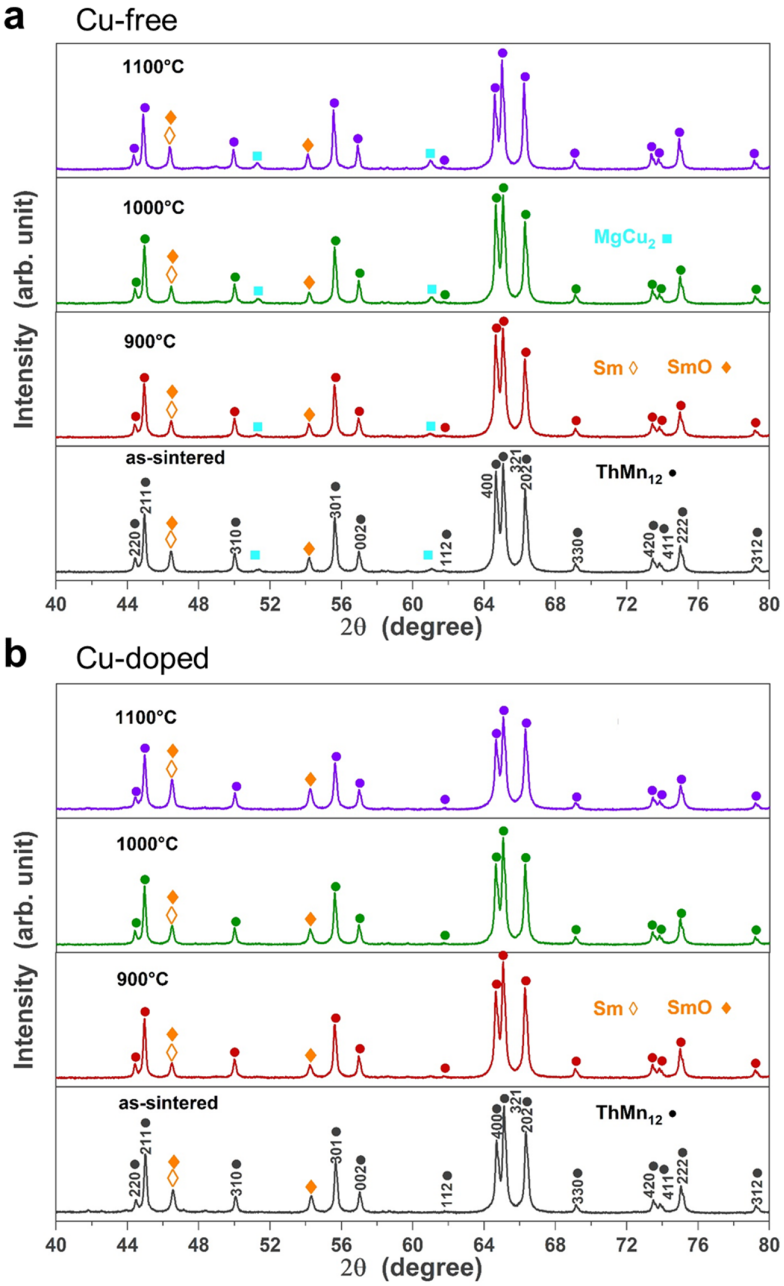

Fig. 2. XRD profiles of as-sintered and post-sinter annealed (a) Cu-free and (b) Cu-doped magnets. XRD was conducted on sintered magnets after pulverization to powder.

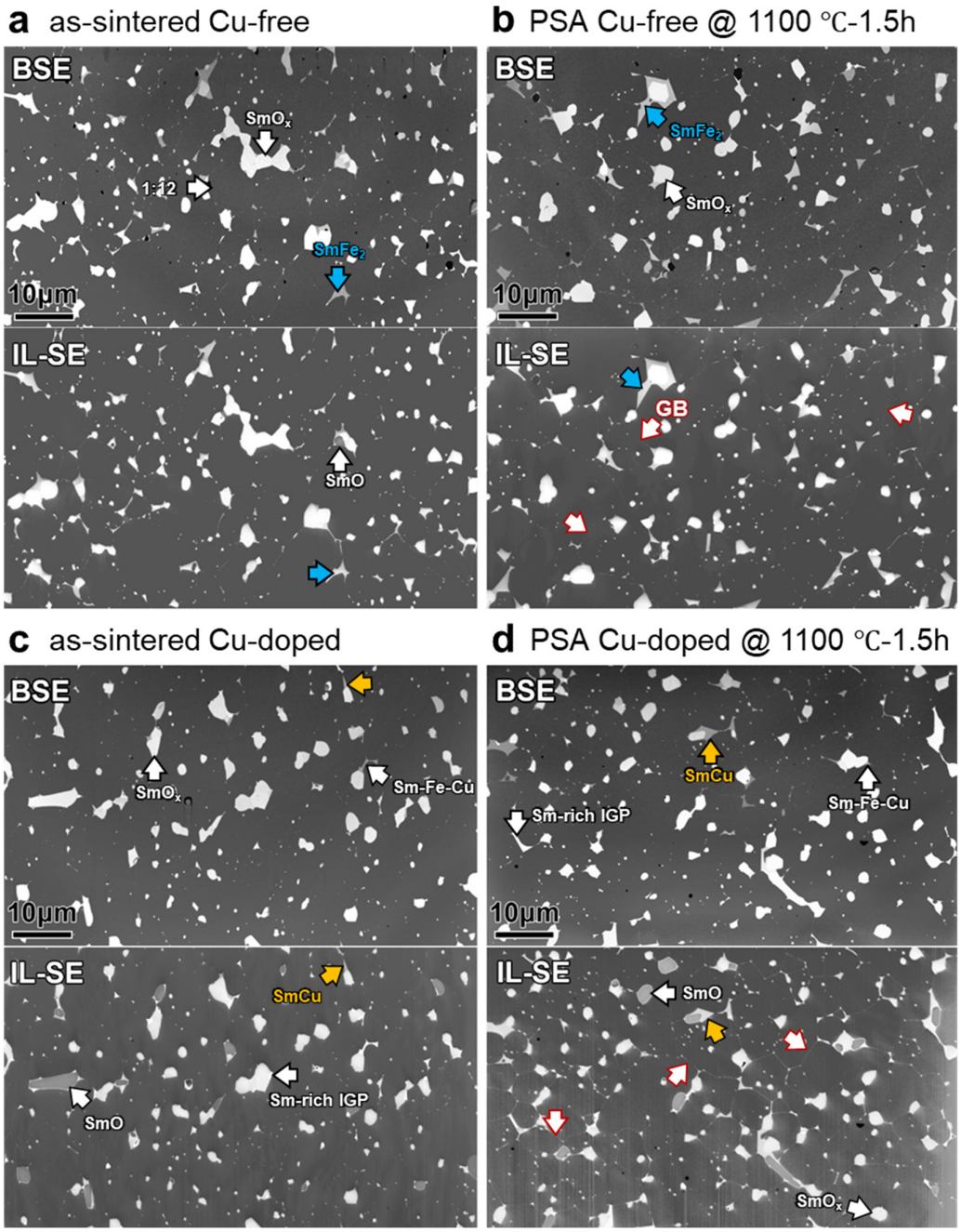

Fig. 3. Backscattered electron (BSE) and In-Lens secondary electron (IL-SE) SEM images of the as sintered (a) Cu-free and (c) Cu-doped magnet, (b) Cu-free magnet and (d) Cu-doped magnet after post-sinter annealing at 1100 ℃ for 1.5 h. $SmFe_2$ and SmCu phases are pointed out by arrows in cyan and orange color.

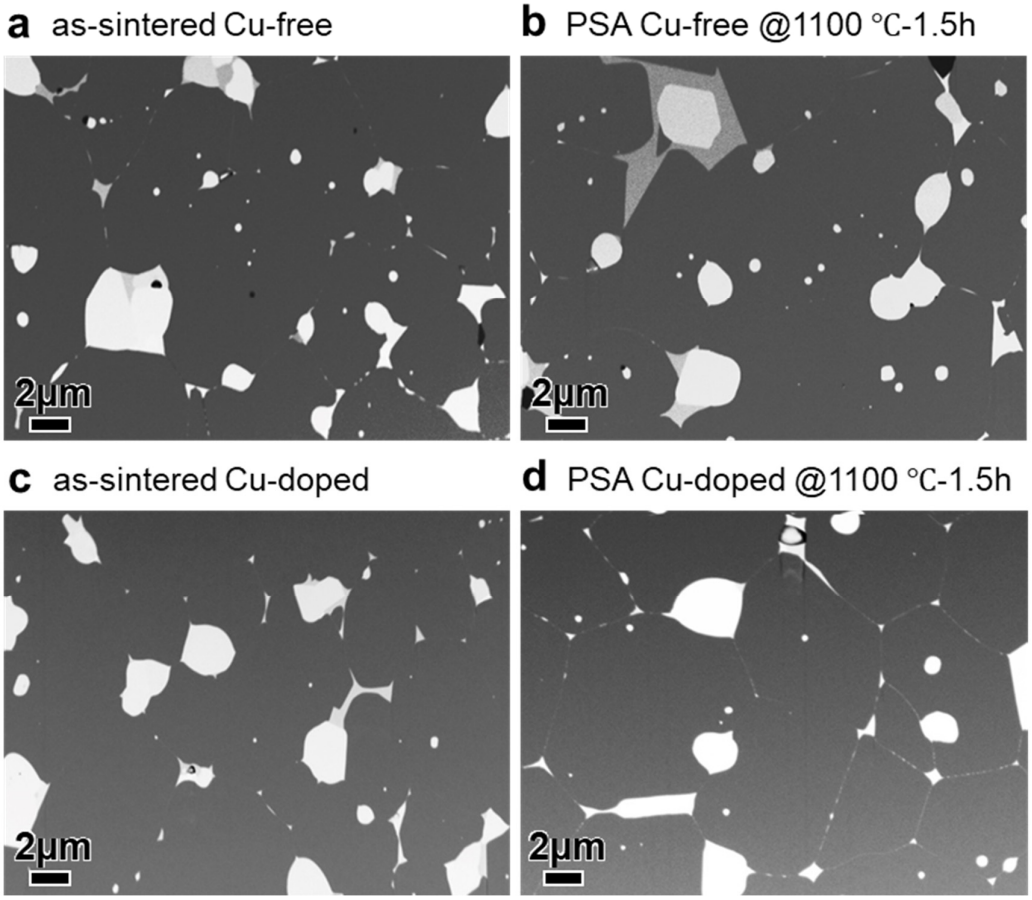

Fig. 4. High magnification backscattered electron (BSE) SEM images of the as sintered (a) Cu-free and (c) Cu-doped magnet, (b) Cu-free magnet and (d) Cu-doped magnet after post-sinter annealing at 1100 ℃ for 1.5 h.

The distribution of secondary phases was examined by SEM. Fig. 3 shows the overall microstructure of the as-sintered and post-sinter annealed (1100°C for 1.5 h) Cu-free and Cu-doped magnets. To specifically illustrate the evolution of the grain boundary structure, the high-magnification BSE images of the corresponding samples are showing in Fig. 4. The average grains size was determined by measuring all grain sizes in the low magnification SEM images. We found the grain size of the 1:12 phase is slightly increased from 4.6 μm and 4.1 μm for the as-sintered Cu-free and Cu-doped magnets to 5.1 μm and 4.8 μm after post-sinter annealing, respectively. This suggests that the addition of Cu does not change the grain size, and there is no distinct grain coarsening during post-sinter annealing at 1100 ℃ for 1.5 h. In the annealed Cu-free

sample shown in Figs. 3b and 4b, the intergranular phase (IGP) is visible in some areas, but it exhibits a weak contrast and limited coverage on the 1:12 phase grains. In contrast, the Cu-doped sample shows the formation of a continuous IGP with bright contrast in the SEM images, surrounding the 1:12 phase as shown in Figs. 3d and 4d. This could be attributed to the improved wettability of the Sm-rich phase in the Cu-doped sample. Therefore, we focused on identifying the various types of Sm-rich phases to understand the role of Cu in the formation of a continuous IGP.

The combination of back scattered electron (BSE) and in-lens secondary electron (IL-SE) imaging was conducted to identify different types of Sm-rich intergranular phases based on the phase contrast. This method has been used for identification of rare-earth (RE)-rich phases in different systems such as $SmFe_{12}$ type or Nd-Fe-B type sintered magnets [22-24, 34-36]. Generally, all four magnets share three types of phases: main 1:12 phase with dark grey contrast, SmO phase, and SmO_x phase. Note that both types of Sm oxides appear with bright contrast in the BSE images, but the SmO phase shows darker contrast than the SmO_x phase in the IL-SE images. In the Cu-free magnet, a gray contrast phase, indicated by cyan arrows, is brighter than the dark 1:12 phase in both BSE and IL-SE images, which could be the $MgCu_2$-type $SmFe_2$ phase and is present in both as-sintered and optimally annealed magnets. This is also confirmed by the XRD results as shown in Figure 2. In contrast, in the Cu-doped sample, we also detect the gray contrast phase indicated by orange arrows in both BSE and IL-SE images. However, the XRD results in Fig. 2 indicate that there is no $SmFe_2$ phase in the Cu-doped magnet. For a better clarity, we further analyzed the structure and chemical compositions of the secondary phases using TEM.

Fig. 5 shows the comparison of the microstructure of the Cu-doped magnets annealed at 1100 ºC for different times. Increasing the annealing time from 1.5 h to 3 h leads to remarkable grain growth. In addition, the Sm-rich IGP seems to be expelled from the thin intergranular region into the triple junctions. Hence, the weaker contrast is observed from the IGPs and the coercivity is reduced from 1.5 T for 1.5 h to 1.03 T for 3 h.

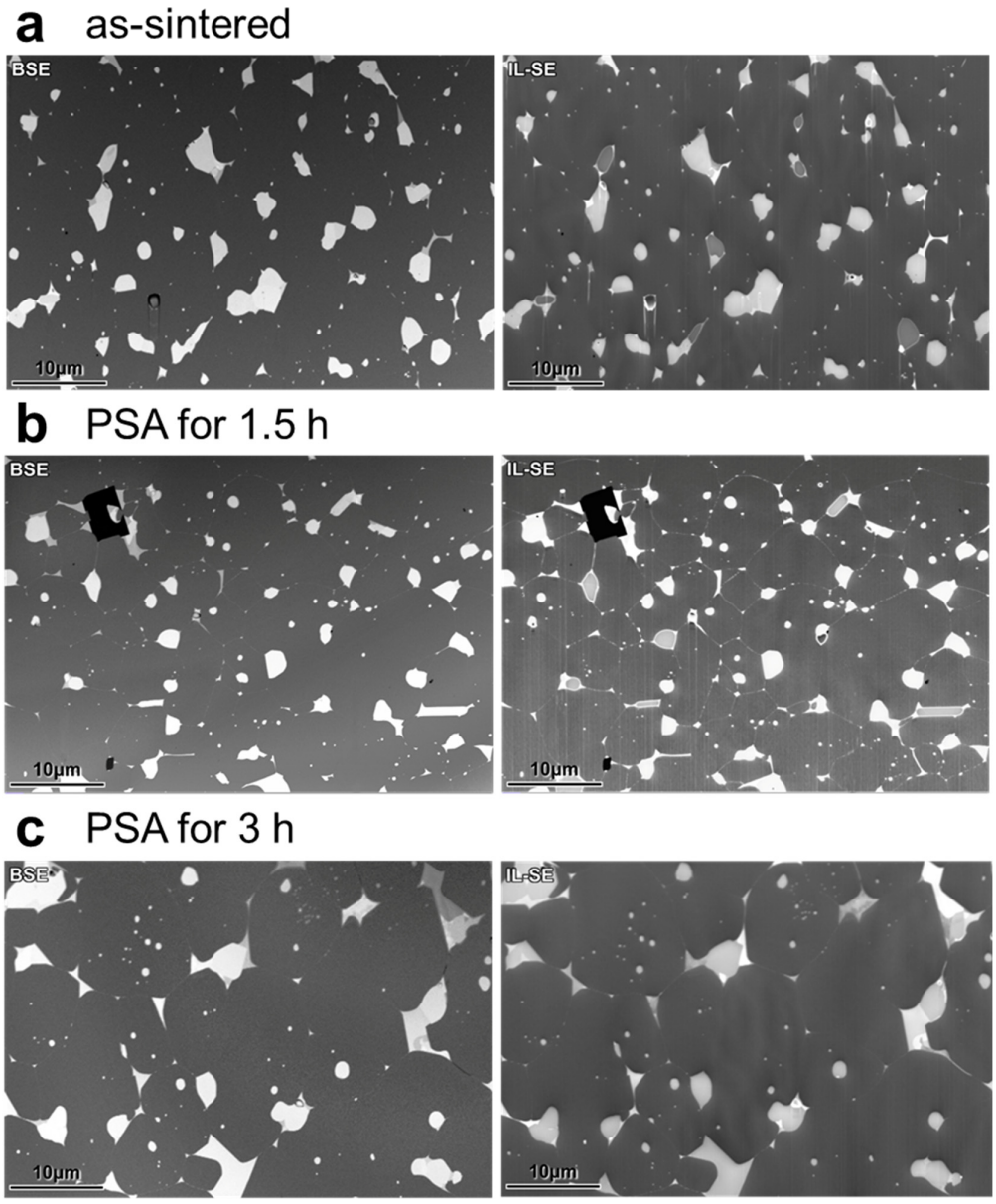

Fig. 5. Backscattered electron (BSE) SEM and In-Lens secondary electron (IL-SE) images of Cu-doped samples (a) in as-sintered condition and post-sinter annealed at 1100 ℃ for (b) 1.5 h and (c) 3 h.

3.3. Structure and chemical composition of Sm-rich phase

The distribution and compositions of the Sm-rich phases in the as-sintered and post-sinter annealed (at 1100℃ for 1.5 h) Cu-doped samples were investigated by SEM, STEM-EDS and are summarized in Table 1. As shown in Fig. 6a for the as-sintered Cu-doped sample, the intergranular phases, Sm-Fe-Cu phase and Sm-rich phase, were

mostly found in the triple junction. The grain boundaries are invisible and discontinuous. After the post-sinter annealing, Sm-Cu-rich IGP not only forms at the triple junction but also infiltrates into the grain boundaries, as presented in Fig. 6a and 6b. The Sm-rich layer at thin grain boundary becomes well-defined, very smooth and continuous. In the STEM-EDS maps of Sm, Fe, Ti, Cu, and O, shown in Fig. 6b, five different Sm-rich phases were identified in both magnets: the SmO phase, the SmO_x phase, the metallic Sm phase, the Sm-Fe-Cu phase, and the Sm-Cu-rich phase. The nanobeam electron diffraction (NBED) patterns of these Sm-rich phases are shown in Fig. 6c. In regions I and A, where the Sm and O contents are 48.4 at.% and 46.2 at.%, respectively (see Table 1), the phase is identified as the *fcc*, $Fm\bar{3}m$, NaCl-type SmO phase. The metallic Sm phase, marked as III and C in Fig. 6b, has a high concentration of Sm and a trace amount of Fe (~4 at.% - 7 at.%), indicating its non-ferromagnetic nature. The NBED patterns for this phase can be indexed to a hexagonal close-packed Mg-type crystal structure (P63/mmc). The Sm-rich phases with a high Cu content are mainly located at the triple junctions in both magnets, such as regions IV and V in the as-sintered magnet and D and E in the post-sinter annealed magnet. Based on the compositions shown in Table 1, the phases with different Cu concentrations correspond to the metallic Sm-Fe-Cu phase and Sm-Cu phase, respectively. These phases are likely to appear as gray contrast in both BSE and in-lens images in Figs. 2c and 2d. Further NBED analysis reveals that the Sm-Fe-Cu phase and Sm-Cu phase can be indexed as *fcc* and CsCl-type structures, respectively. Note that Sepehri-Amin *et al.* [36] and Sasaki *et al.* [34] have reported similar metallic Nd-Co-Cu-rich and Nd-Cu-rich triple junction phases in as-sintered and optimally annealed Nd-Fe-B sintered magnets, which agrees with the structures of the Sm-Fe-Cu and Sm-Cu phases observed in the $SmFe_{12}$-based sintered magnets. In addition, the EDS results in Table 1 show that the metallic Sm-Fe-Cu phase contains ~20 at.% of Fe, while the Sm-Cu phase has a very low Fe content of ~2 at.% - 3 at.%, suggesting that these are likely to be non-ferromagnetic phases. In contrast to the as-sintered magnet, the Sm-Cu phase in the annealed magnet extends from the triple junctions to form a thin Sm and Cu enriching intergranular phase

(IGP), as marked by red arrows in Fig. 6b, effectively smooth the grain interfaces and isolating the 1:12 grains. Compared to the microstructure of the Cu-free magnet, the primary effect of Cu is to suppress the formation of $SmFe_2$ and promote the formation of Fe-lean Sm-Cu phases with good wettability. It should be noted that while the composition of the Cu-rich phase at triple junctions does not significantly change upon annealing shown in Table 1, a notable increase in Cu content is observed in the thin intergranular phases—increasing from almost 0 at.% (region marked by yellow arrowhead in Fig. 6b)in the as-sintered state to approximately 3.4 at.% (region marked by red arrowhead in Fig. 6b) after optimal annealing, which is evident in STEM-EDS maps shown in Fig. 6b. More detailed information on the composition of thin IGP will be investigated using High-resolution HAADF-STEM.

Table 1 Chemical composition (at.%) of the marked phases in Fig. 5(a) and 5(b) for Cu-doped magnets.

As-sintered			**1100 °C-1.5h**		
Area	STEM-EDS composition (at.%)	Phase	Area	STEM-EDS composition (at.%)	Phase
I	$Sm_{48.4}O_{46.2}Fe_{1.8}Ti_{0.3}V_{0.4}Al_{2.5}Cu_{0.4}$	SmO	A	$Sm_{45.7}O_{47.7}Fe_{1.9}Ti_{0.4}V_{0.5}Al_{2.2}Cu_{1.6}$	SmO
II	$Sm_{65.1}O_{27.6}Fe_{2.6}Ti_{0.4}V_{0.5}Al_{3.3}Cu_{0.5}$	SmO_x	B	$Sm_{55.3}O_{23.7}Fe_{11.8}Ti_{0.7}V_{0.5}Al_{7.4}Cu_{0.6}$	SmO_x
III	$Sm_{70.6}Fe_{6.4}Ti_{0.6}V_{0.8}Al_{6.1}Cu_{10.2}O_{5.3}$	Metallic Sm	C	$Sm_{79.8}Fe_{4.3}Ti_{0.1}V_{0.6}Al_{2.8}Cu_{2.8}O_{9.6}$	Metallic Sm
IV	$Sm_{49.8}Fe_{23.1}Cu_{11.5}Ti_{0.4}V_{0.8}Al_{8.6}O_{5.8}$	Sm-Fe-Cu	D	$Sm_{55.2}Fe_{16.7}Cu_{12.0}Ti1.3V_{1.0}A_{18.7}O_{5.1}$	Sm-Fe-Cu
V	$Sm_{46.4}Cu_{41.1}Fe_{3.2}Ti_{0.6}V_{0.7}Al_{6.6}O_{1.4}$	Sm-Cu	E	$Sm_{46.1}Cu_{38.5}Fe_{2.7}Ti_{0.4}V_{0.3}Al_{6.6}O_{5.4}$	Sm-Cu

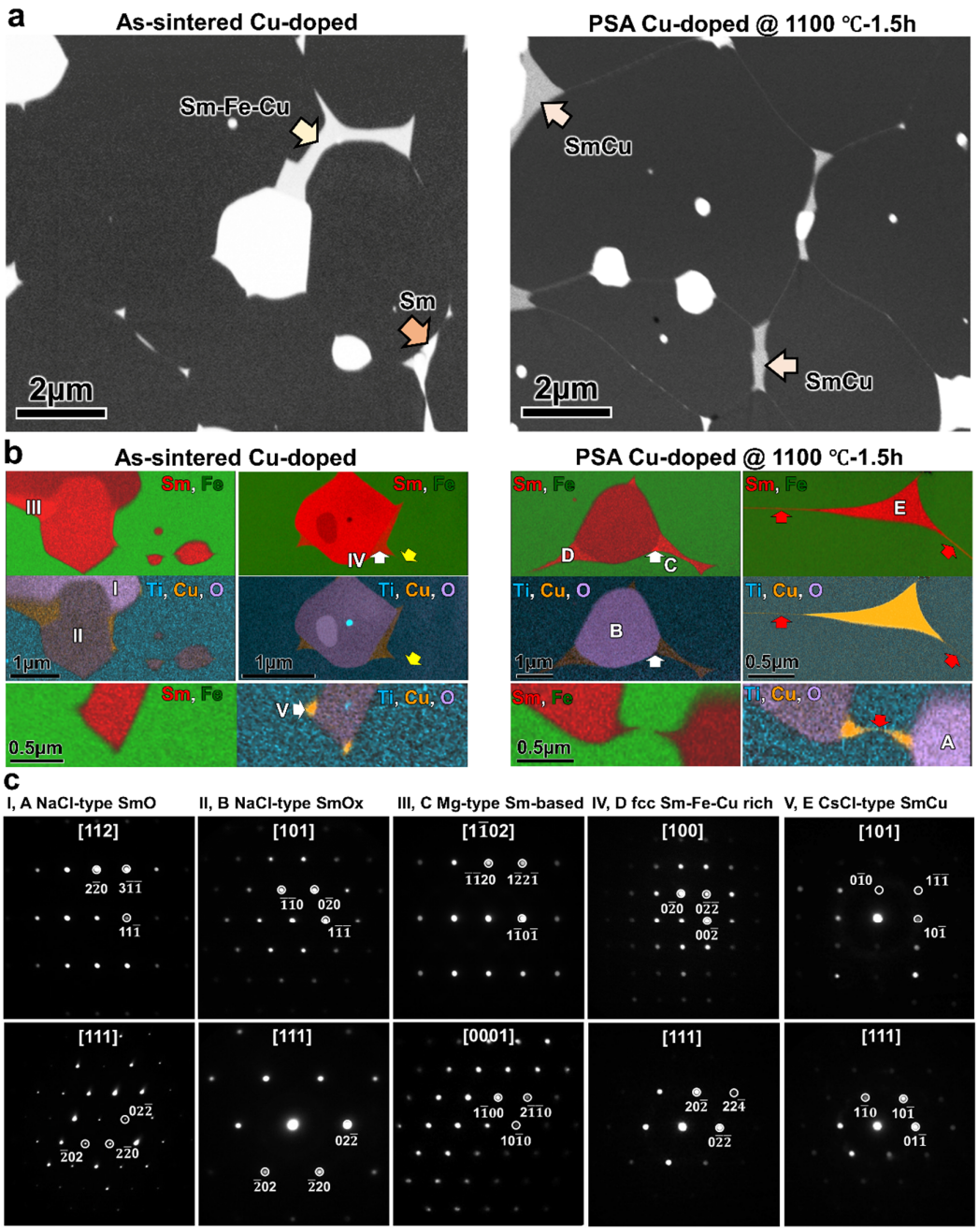

Fig. 6. (a) High magnification backscattered electron (BSE) SEM images, (b) STEM-EDS maps of Sm, Fe and Ti, Cu, O; (c) the sets of nano-beam electron diffraction patterns obtained from the different regions in the maps for as-sintered Cu-doped magnet and post-sinter annealed Cu-doped magnet under 1100 ℃ for 1.5 h.

In this section, we discuss why only a small coercivity increase is achieved in the Cu-free magnet upon annealing. Fig. 7 shows the TEM analysis of the intergranular

region, the triple junction phases and the magnetic domain for the optimally annealed Cu-free magnet. As shown in Fig. 7a, the formation of Sm-rich intergranular phase along the grain boundary was confirmed. However, the STEM-EDS map for this thin IGP reveals its discontinuity, as also observed by SEM image in Fig. 2b. The compositional analysis from the discontinuous region (marked by arrow) indicates that a considerably high Fe concentration of around 70 at. % in this region shown in Fig. 7a. In the Sm+Fe EDS map of Fig. 7b, the region in the white solid-lined box with Fe+Al concentration of around 64 at.% could be the $SmFe_2$ phase. This is further supported by nano-beam electron diffraction (NBED) patterns obtained from the selected region in Fig. 7b. It should be noted that the formation of the $SmFe_2$ phase consumes the excess Sm needed for the formation of Sm-rich IGP and causes the discontinuity of the IGP in the Cu-free sample, even after optimal annealing. To investigate whether the $SmFe_2$ phase itself exhibits any magnetization or not; we observed magnetic domain wall in the $SmFe_2$ phase using Lorentz TEM (L-TEM). A domain wall within the $SmFe_2$ phase is clearly visible in Lorentz Fresnel mode as shown in Fig. 7c. This domain wall traverses the interface between the $SmFe_2$ phase and the 1:12 phase and connects directly to the 1:12 matrix phase. Upon application of an external magnetic field, the domain wall within the $SmFe_2$ phase moves while that in the 1:12 matrix phase remains relatively stable. This suggests that the ferromagnetic nature of the $SmFe_2$ phase, which could be a weak point during the magnetization reversal process, results in limited coercivity enhancement in the Cu-free magnet after an optimal annealing process.

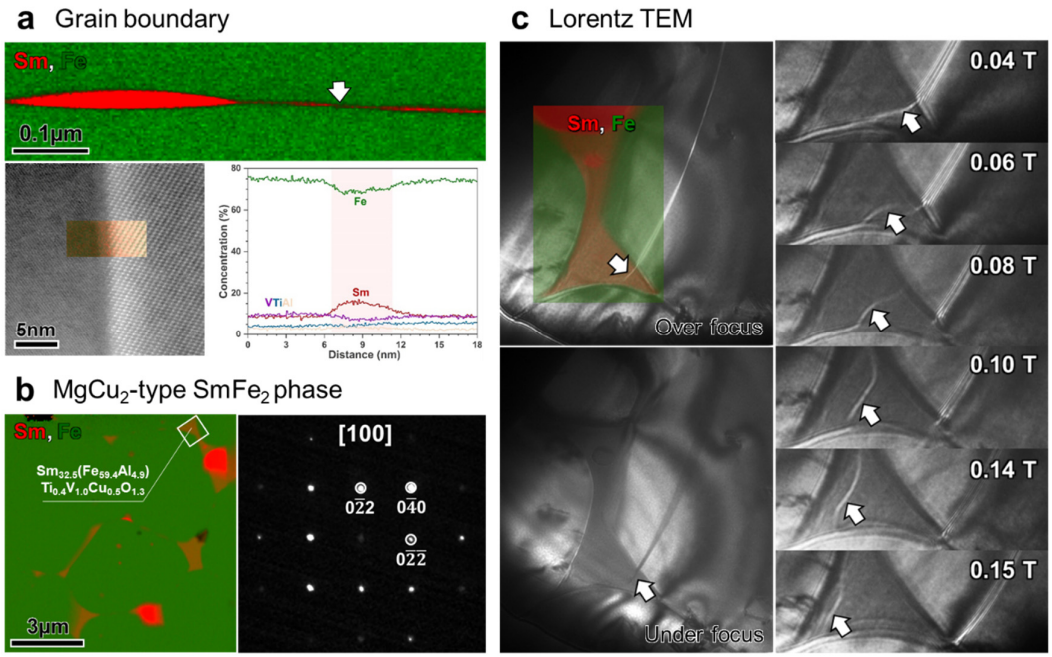

Fig. 7. (a) Low magnification STEM-EDS map of Sm and Fe, high-resolution HAADF-STEM image super-imposed with EDS map for thin intergranular phase, and the compostional profile across the thin intergranular phase; (b) STEM-EDS map of Sm and Fe, and the composition in atomic percent and the nano-beam electron diffraction pattern obtained from the selected region (white box) in the EDS map; (c) Magnified Lorentz TEM images super-imposed with EDS map, Lorentz TEM images at various magnetic fields for Cu-free magnet after post-sinter annealing at 1100 ℃ for 1.5 h.

The most obvious microstructural difference upon annealing is the formation of continuous IGP enveloping the 1:12 phase grains in the Cu-doped magnet. Here, we compare the morphology of the grain interfaces and the chemical composition of the IGP phase in the as-sintered and the optimally annealed Cu-doped magnets. Fig. 8 shows the high-resolution HADDF-STEM images, the superimposed STEM-EDS maps, and the corresponding compositional line profiles. As shown in Fig. 8a, 8b and 8c, 8d. The thin IGP layers with thickness of about ~2-3 nm were observed in both magnets. However, the IGPs shown in Figs. 8c and 8d for the annealed sample is extremely smooth and regular. In addition, the thin layers contain much lower Fe content, much higher Cu content and much enriched with Sm compared to those of the

as-sintered sample. The ferromagnetic Fe content of ~10 at.% in *c*-plane IGP and ~35 at.% in side-plane IGP for the annealed Cu-doped sample, which is in agreement with the previously report for the $Sm_8Fe_{73.5}Ti_8V_8Al_2Cu_{0.5}$ magnet [24], dramatically reduces the magnetic coupling between the adjacent 1:12 phases. In contrast, the Fe content in IGPs for the as-sintered Cu-doped magnet is too high, ~55 at.% in *c*-plane and ~70 at.% in side-plane IGPs, respectively, indicating stronger exchange coupling by ferromagnetic IGPs. Furthermore, Cu concentration in the IGP layers increases from ~4 at.% to ~7.5 at.% in the *c*-plane IGP and from ~1.5 at.% to ~5 at.% in the side-plane IGP. This indicates an infiltration of Sm-Cu-rich IGP into the grain boundaries. The Cu enrichment in the Sm-rich IGP not only reduces Fe content within the IGP but also enhances its wettability, enabling smoother and more continuous interfaces resulting in a larger coercivity.

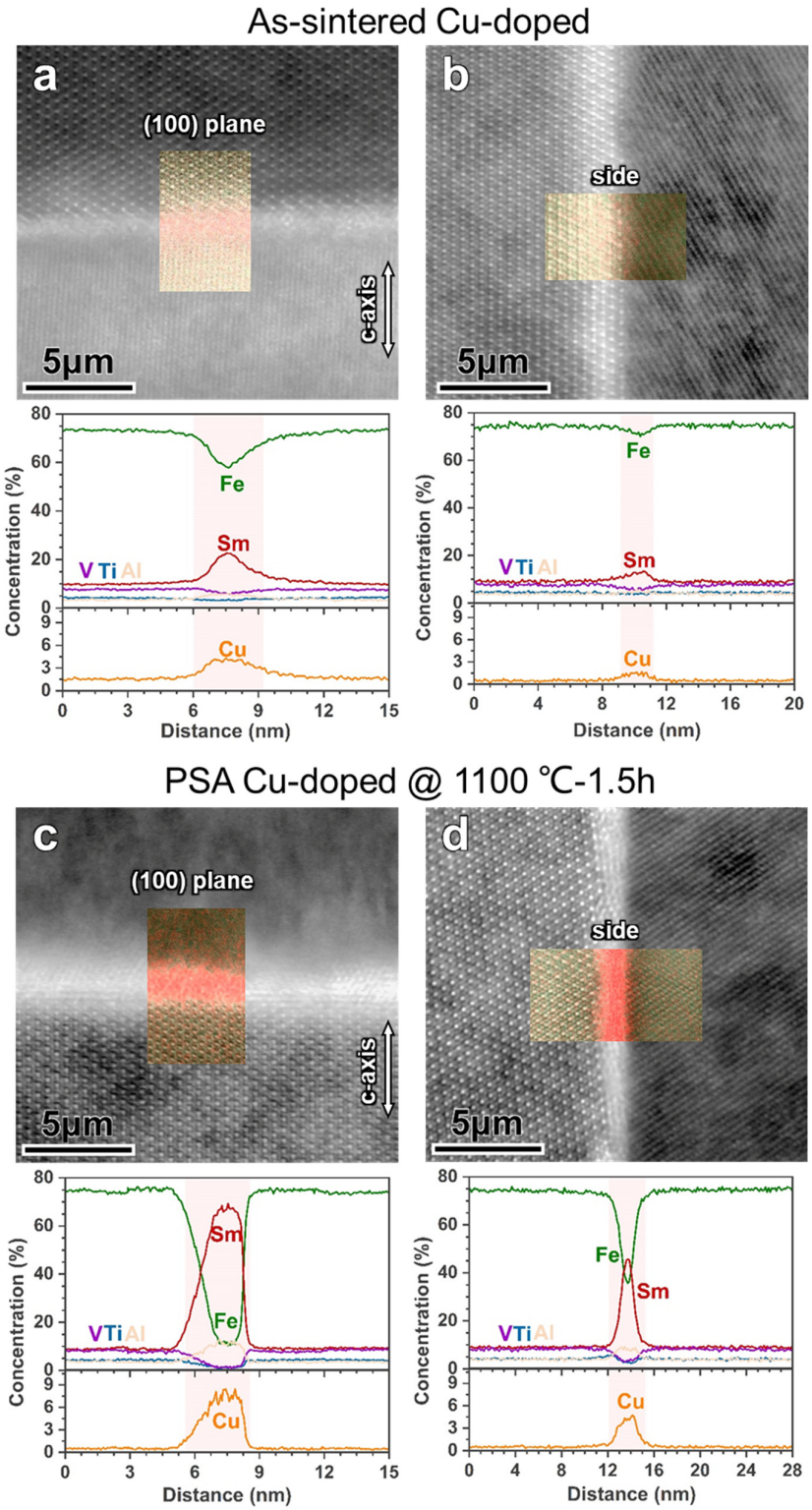

Fig. 8. High-resolution HAADF-STEM images super-imposed with EDS maps of Sm and Fe, and the corresponding composition line profiles obtained from c-plane and side-plane IGPs for (a), (b) as-sintered and c), d) post-sinter annealed Cu-doped magnets.

4. Discussion

In this work, we investigated the effect of annealing process on the microstructure and coercivity of the Cu-free and Cu-doped $Sm(Fe,Ti,V)_{12}$-based sintered magnets by detailed microstructure analysis. In the Cu-free system, the annealing process only brings about a minor coercivity increase of 0.1 T. In contrast, the coercivity of the Cu-doped $Sm(Fe,Ti,V)_{12}$ sintered magnet increase from 0.9 T to ~1.5 T, reaching the highest value reported so far. This enhancement is due to the formation of continuous Fe-lean IGP that weaken the exchange-coupling between the main phases, similar to the well-investigated Nd-Fe-B system [33, 37, 38]. In the Cu-free magnets, the $SmFe_2$ phase is distributed throughout the microstructure as a triple junction phase (shown in Fig. 3 and Fig. 7), which is consistent with the observations in the sintered $Sm(Fe,V)_{12}$ magnet [21]. The XRD profiles shown in Fig. 2a clearly demonstrate the presence of the $SmFe_2$ phase in all the Cu-free samples, regardless of the annealing conditions. Interestingly, the negative effect of the ferromagnetic $SmFe_2$ phase on coercivity is not apparent in the as-sintered magnets, likely due to strong exchange coupling between grains through the continuous Fe-rich intergranular phase. It should be noted that the $SmFe_2$ phase is a ferromagnetic phase with a low anisotropy field, $\mu_0 H_a$ of 1.2 T, the saturation magnetization, $\mu_0 M_s$, of ~0.56 T at 300 K and Curie temperature T_c of ~670 K [40-42]. These intrinsic magnetic properties make the $SmFe_2$ phase being a nucleation site and facilitate the magnetization reversal process. The domain wall in the $SmFe_2$ phase easily displaced under the application of a small external field, as shown in Fig. 7c. In addition, the formation of the $SmFe_2$ phase consumes too much of the Sm required for the formation of Sm-rich IGPs, similar to the effect of $CeFe_2$ phase in the $Ce_2Fe_{14}B$ magnet [43]. This may be one of the reasons for the observed discontinuity of the IGP covering the matrix phase (Fig. 7). In this work, we show that the detrimental $SmFe_2$ phase can be suppressed by the addition of Cu as shown in Fig. 7b. Instead, the Sm-Cu-based phases are formed in the microstructure of Cu-doped samples as shown in the SEM images in Fig. 3c-d and the TEM results in Fig. 6. Based on the results obtained from Differential Thermal Analysis (DTA) measurements on both the as-

sintered and optimally annealed magnets for the Cu-free and Cu-doped samples, as shown in Fig. S5, the endothermic peak associated with the Sm-rich phase becomes pronounced and shifts to a lower temperature—by approximately 100 °C—after Cu addition. This indicates that Cu effectively lowers the melting point of the Sm-rich phase, leading to form Sm-Cu-based phases with high diffusivity and good wettability on surface of $SmFe_{12}$-based grains, and contributes to the formation of continuous Fe-lean, Cu-rich IGPs during the optimal annealing process (see Figs. 4d 6b, and 8d). HRTEM observations of the grain boundaries in the post-sinter annealed Cu-containing magnet, as shown in Fig. 8, the annealed sample exhibits a Cu-rich, Fe-lean composition in the IGP, with Cu concentrations of ~7.5 at.% in the *c*-plane and ~5 at.% in the side-plane IGP. These changes indicate enhanced wettability due to microalloying with Cu. These result in a high coercivity of 1.5 T in the Cu-doped sintered magnet. Therefore, further reduction of Fe concentration at the side-plane IGP is expected to further increase in the coercivity. From this perspective, composition optimization by trace addition of Ga, Zn, and GBs modification by two-alloy method or infiltration of low-melting eutectic alloys such as Cu-Ga, Sm-Cu, Sm-Al-Cu should be potential to achieve desired microstructure and higher coercivity.

Another interesting observation in this work is the required high optimal annealing temperature of 1100 ºC, which is much higher than that (~480 - 750 ºC) for the Nd-Fe-B sintered magnets. This indicates a different mechanism for the formation of Sm-rich IGPs. In the Nd-Fe-B system, as proposed by Sepehri-Amin *et al*. [32], the low eutectic point Nd-Cu based alloys in the triple junction infiltrate into the thin IGP during the annealing process to achieve better magnetic isolation among the 2:14:1 phase grains and thereby increase the coercivity. In the case of Nd-Fe-B sintered magnets, Nd-rich intergranular phases (IGPs) are typically present in the as-sintered state. Post-sinter annealing near the Nd-Cu eutectic temperature promotes wetting and homogenization of these IGPs, leading to well-defined grain boundaries and high coercivity [33]. In contrast, in $SmFe_{12}$-based magnets, particularly those doped with Cu, the Sm-Cu IGPs are rarely observed at interfaces between matrix phase (mainly locates at triple

junctions) immediately after sintering. The formation of IGPs that isolates matrix grains requires a reaction between the $SmFe_{12}$-based matrix, residual metallic Sm, and a Sm–Fe–Cu ternary phase. This reaction only occurs at elevated temperatures (~1100 °C), where the Sm-rich liquid phase is in equilibrium with the $ThMn_{12}$-type main phase [44, 45]. This temperature is well above the Sm–Cu eutectic point (~600–650 °C) [46] , suggesting that high-temperature annealing is essential for effective formation and redistribution of the Sm-Cu IGP. Furthermore, annealing at ~1100 °C ensures sufficient diffusion of Sm and Cu to the grain boundary regions, which is critical for forming a continuous IGP network. These observations explain why the optimal post-sinter annealing temperature remains unchanged even after Cu addition—both composition and heat treatment should be tailored to achieve desirable IGP formation and high coercivity. Therefore, designing the optimum post-sinter annealing condition based on different compositions is also crucial for achieving higher coercivity in the $SmFe_{12}$-based sintered magnets.

Based on the above discussion, Fig. 9 schematically illustrates the microstructure evolution for the Cu-free and Cu-doped $Sm(Fe,Ti,V)_{12}$-based sintered magnet by post-sinter annealing. In the as-sintered Cu-free magnet shown in Fig. 9a, the ferromagnetic $SmFe_2$ phase is distributed in the microstructure as a triple-junction phase. In addition, due to the presence of Fe-rich IGP, the 1:12 grains are exchange coupled even after post-sintering annealing, resulting in low coercivity. In contrast, when Cu is alloyed into the magnet, the formation of the $SmFe_2$ phase is suppressed. Instead, Sm-rich phases, including metallic Sm, Sm-Fe-Cu and Sm-Cu are formed at triple junction shown in Fig. 9b. Upon post-sinter annealing, the Sm-rich phases, which are in equilibrium with the 1:12 phase, form in the grain boundary region. The addition of Cu also improves the wettability of Sm-rich phase, leading to the formation of a continuous, Fe-lean IGP that envelops the matrix phase. This is the major reason for the achieved high coercivity in the post-sinter annealed Cu-doped magnet.

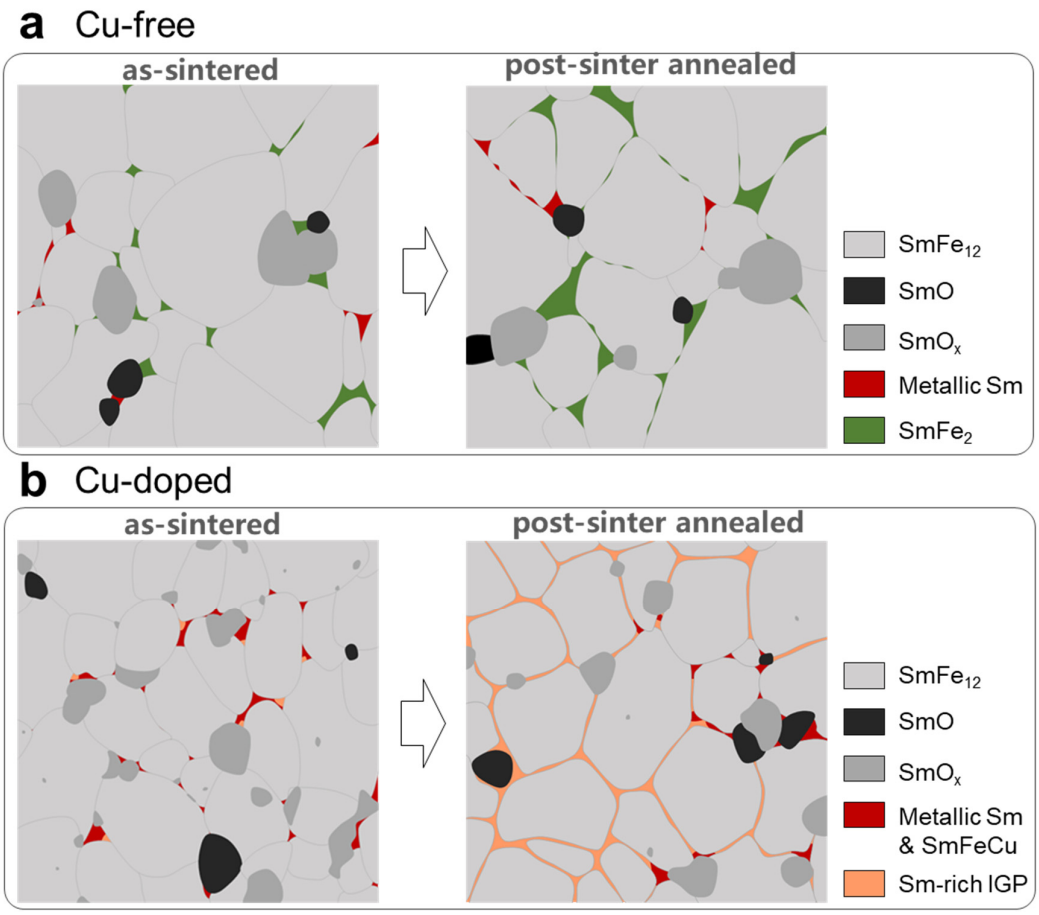

Fig. 9. Schematic illustrations for the microstructure evolution for (a) Cu-free and (b) Cu-doped sintered $SmFe_{12}$-based magnets by post-sinter annealing.

5. Conclusions

In this work, we demonstrated a significant increase in coercivity ($\mu_0 H_c$) from 0.9 T to 1.5 T in Cu-doped $Sm(Fe,Ti,V)_{12}$-based sintered magnets through post-sinter annealing. The Cu-doped magnet also exhibits larger remanence ($\mu_0 M_r$) of 0.71 T and maximum energy product ($(BH)_{max}$) of 84 kJ/m³. Detailed characterization using FIB/SEM, Lorentz TEM, and STEM/EDS revealed the microstructural origins of this improvement. The high optimum annealing temperature of 1100 ºC for both Cu-free and Cu-doped magnets confirms the importance of maintaining equilibrium between the Sm-rich phase and the $SmFe_{12}$-based main phase in promoting the formation of Sm-rich intergranular phases (IGPs). Additionally, further analysis shows that the formation

of continuous IGPs is influenced not only by the annealing temperature but also by the composition of the magnet.

We identified two key roles of Cu in enhancing the coercivity: (1) the addition of Cu effectively suppresses the formation of the ferromagnetic $SmFe_2$ phase, which could serve as a nucleation site for magnetization reversal, thereby improving the coercivity. (2) Cu doping promotes the formation of the desirable Mg-type Sm-rich phase and the CsCl-type SmCu phase with improved wettability. This leads to the formation of thick, continuous, Fe-lean IGPs during optimal annealing process, which decouple the $SmFe_{12}$-based matrix grains and play a key role in the substantial increase in coercivity in the Cu-doped magnets.

This study establishes a clear process-dependent relationship between microstructure and coercivity in the $SmFe_{12}$-based sintered magnets, thus providing guidelines for the design and development of high-performance $SmFe_{12}$-based anisotropic bulk magnets for practical applications.

Declaration of Competing Interest

The authors declare that they have no known competing financial interests or personal relationships that could have appeared to influence the work reported in this paper.

Acknowledgments

The authors acknowledge Y. Toyooka, H. Sebata, and N. Kurata for technical supports. This work was in-part supported by JSPS KAKENHI Grant Number JP23H01674, MEXT Program: Data Creation and Utilization-Type Material Research and Development Project (Digital Transformation Initiative Center for Magnetic Materials) Grant Number JPMXP1122715503, and JST-ERATO “Magnetic Thermal Management Materials” (Grant No. JPMJER2201).

References

[1] A. Gabay, G. Hadjipanayis, Recent developments in RFe_{12}-type compounds for permanent magnets, Scripta Materialia 154 (2018) 284-288.

[2] Y. Hirayama, Y. Takahashi, S. Hirosawa, K. Hono, Intrinsic hard magnetic properties of Sm $(Fe_{1-x}Co_x)_{12}$ compound with the $ThMn_{12}$ structure, Scripta Materialia 138 (2017) 62-65.
[3] K. Ohashi, Y. Tawara, R. Osugi, M. Shimao, Magnetic properties of Fe-rich rare-earth intermetallic compounds with a $ThMn_{12}$ structure, Journal of applied physics 64(10) (1988) 5714-5716.
[4] S. Cheng, V. Sinha, Y. Xu, J. Elbicki, E. Boltich, W. Wallace, S. Sankar, D. Laughlin, Magnetic and structural properties of $SmTiFe_{11-x}Co_x$ alloys, Journal of magnetism and magnetic materials 75(3) (1988) 330-338.
[5] I. Tereshina, N. Kostyuchenko, E. Tereshina-Chitrova, Y. Skourski, M. Doerr, I. Pelevin, A. Zvezdin, M. Paukov, L. Havela, H. Drulis, ThMn12-type phases for magnets with low rare-earth content: Crystal-field analysis of the full magnetization process, Scientific reports 8(1) (2018) 3595.
[6] P. Tozman, H. Sepehri-Amin, K. Hono, Prospects for the development of $SmFe_{12}$-based permanent magnets with a ThMn12-type phase, Scripta Materialia 194 (2021) 113686.
[7] G. Hadjipanayis, A. Gabay, A. Schönhöbel, A. Martín-Cid, J. Barandiaran, D. Niarchos, $ThMn_{12}$-type alloys for permanent magnets, Engineering 6(2) (2020) 141-147.
[8] Y. Takahashi, H. Sepehri-Amin, T. Ohkubo, Recent advances in $SmFe_{12}$-based permanent magnets, Science and Technology of Advanced Materials 22(1) (2021) 449-460.
[9] T.B. Massalski, H. Okamoto, P. Subramanian, L. Kacprzak, W.W. Scott, Binary alloy phase diagrams, American society for metals Metals Park, OH1986.
[10] K. Buschow, Permanent magnet materials based on tetragonal rare earth compounds of the type $RFe_{12-x}M_x$, Journal of magnetism and magnetic materials 100(1-3) (1991) 79-89.
[11] H.S. Li, J. Coey, Magnetic properties of ternary rare-earth transition-metal compounds, Handbook of magnetic materials 6 (1991) 1-83.
[12] K. Buschow, Structure and properties of some novel ternary Fe-rich rare-earth intermetallics, Journal of applied physics 63(8) (1988) 3130-3135.
[13] X. Zhong, F. de Boer, D. de Mooij, K. Buschow, Magnetic coupling in the tetragonal rare earth iron compounds of the type R $(Fe,V)_{12}$, Journal of the Less Common Metals 163(1) (1990) 123-132.
[14] R. Verhoef, F. De Boer, Z. Zhi-dong, K. Buschow, Moment reduction in $RFe_{12-x}T_x$ compounds (R= Gd, Y and T= Ti, Cr, V, Mo, W), Journal of magnetism and magnetic materials 75(3) (1988) 319-322.
[15] K. Kobayashi, S. Suzuki, T. Kuno, K. Urushibata, N. Sakuma, M. Yano, T. Shouji, A. Kato, A. Manabe, The stability of newly developed $(R,Zr)(Fe,Co)_{12-x}Ti_x$ alloys for permanent magnets, Journal of Alloys and Compounds 694 (2017) 914-920.
[16] A. Schönhöbel, R. Madugundo, O.Y. Vekilova, O. Eriksson, H.C. Herper, J. Barandiarán, G. Hadjipanayis, Intrinsic magnetic properties of $SmFe_{12-x}V_x$ alloys with reduced V-concentration, Journal of Alloys and Compounds 786 (2019) 969-974.
[17] J. Coey, Comparison of the intrinsic magnetic properties of $R_2Fe_{14}B$ and $R(Fe_{11}Ti)$; R= rare earth, Journal of magnetism and magnetic materials 80(1) (1989) 9-13.
[18] C. Nan-Xian, H. Shi-qiang, W. Yu, S. Jiang, Phase stability and site preference of $Sm(Fe,T)_{12}$, Journal of magnetism and magnetic materials 233(3) (2001) 169-180.
[19] Y. Harashima, K. Terakura, H. Kino, S. Ishibashi, T. Miyake, First-principles study on stability and magnetism of $NdFe_{11}M$ and $NdFe_{11}MN$ for M= Ti, V, Cr, Mn, Fe, Co, Ni, Cu, Zn, Journal of Applied Physics 120(20) (2016).
[20] X. Tang, J. Li, A. Srinithi, H. Sepehri-Amin, T. Ohkubo, K. Hono, Role of V on the coercivity

of $SmFe_{12}$-based melt-spun ribbons revealed by machine learning and microstructure characterizations, Scripta Materialia 200 (2021) 113925.
[21] K. Otsuka, M. Kamata, T. Nomura, H. Iida, H. Nakamura, Coercivities of Sm-Fe-M sintered magnets with $ThMn_{12}$-type structure (M = Ti, V), Materials Transactions 62(6) (2021) 887-891.
[22] J. Zhang, X. Tang, H. Sepehri-Amin, A. Srinithi, T. Ohkubo, K. Hono, Origin of coercivity in an anisotropic $Sm(Fe,Ti,V)_{12}$-based sintered magnet, Acta Materialia 217 (2021) 117161.
[23] J. Zhang, X. Tang, A. Bolyachkin, A. Srinithi, T. Ohkubo, H. Sepehri-Amin, K. Hono, Microstructure and extrinsic magnetic properties of anisotropic $Sm(Fe,Ti,V)_{12}$-based sintered magnets, Acta Materialia 238 (2022) 118228.
[24] A. Srinithi, X. Tang, H. Sepehri-Amin, J. Zhang, T. Ohkubo, K. Hono, High-coercivity $SmFe_{12}$-based anisotropic sintered magnets by Cu addition, Acta Materialia 256 (2023) 119111.
[25] D. Ogawa, X. Xu, Y. Takahashi, T. Ohkubo, S. Hirosawa, K. Hono, Emergence of coercivity in $Sm(Fe_{0.8}Co_{0.2})_{12}$ thin films via eutectic alloy grain boundary infiltration, Scripta Materialia 164 (2019) 140-144.
[26] A.M. Schönhöbel, R. Madugundo, J.M. Barandiarán, G.C. Hadjipanayis, D. Palanisamy, T. Schwarz, B. Gault, D. Raabe, K. Skokov, O. Gutfleisch, Nanocrystalline Sm-based 1:12 magnets, Acta Materialia 200 (2020) 652-658.
[27] H. Lee, J. Kim, Effect of Cu addition on magnetic properties and microstructures of $SmFe_{11}Ti$ alloys prepared by melt-spinning, 2023 IEEE International Magnetic Conference-Short Papers (INTERMAG Short Papers), IEEE, 2023, pp. 1-2.
[28] W. Li, T. Ohkubo, K. Hono, Effect of post-sinter annealing on the coercivity and microstructure of Nd-Fe-B permanent magnets, Acta Materialia 57(5) (2009) 1337-1346.
[29] T. Woodcock, F. Bittner, T. Mix, K.-H. Müller, S. Sawatzki, O. Gutfleisch, On the reversible and fully repeatable increase in coercive field of sintered Nd-Fe-B magnets following post sinter annealing, Journal of magnetism and magnetic materials 360 (2014) 157-164.
[30] M. Sagawa, S. Fujimura, N. Togawa, H. Yamamoto, Y. Matsuura, New material for permanent magnets on a base of Nd and Fe, Journal of Applied Physics 55(6) (1984) 2083-2087.
[31] T. Sasaki, Y. Takada, H. Okazaki, T. Ohkubo, T. Nakamura, T. Sato, A. Kato, Y. Kaneko, K. Hono, Role of Ga on the high coercivity of Nd-rich Ga-doped Nd-Fe-B sintered magnet, Journal of Alloys and Compounds 790 (2019) 750-759.
[32] H. Sepehri-Amin, T. Ohkubo, T. Shima, K. Hono, Grain boundary and interface chemistry of an Nd-Fe-B-based sintered magnet, Acta Materialia 60(3) (2012) 819-830.
[33] F. Vial, F. Joly, E. Nevalainen, M. Sagawa, K. Hiraga, K. Park, Improvement of coercivity of sintered NdFeB permanent magnets by heat treatment, Journal of magnetism and magnetic materials 242 (2002) 1329-1334.
[34] T. Sasaki, T. Ohkubo, K. Hono, Structure and chemical compositions of the grain boundary phase in Nd-Fe-B sintered magnets, Acta Materialia 115 (2016) 269-277.
[35] T. Sasaki, T. Ohkubo, K. Hono, Y. Une, M. Sagawa, Correlative multi-scale characterization of a fine grained Nd-Fe-B sintered magnet, Ultramicroscopy 132 (2013) 222-226.
[36] H. Sepehri-Amin, T. Ohkubo, M. Zakotnik, D. Prosperi, P. Afiuny, C. Tudor, K. Hono, Microstructure and magnetic properties of grain boundary modified recycled Nd-Fe-B sintered magnets, Journal of Alloys and Compounds 694 (2017) 175-184.
[37] R.K. Mishra, J. Chen, G. Thomas, Effect of annealing on the microstructure of sintered Nd-Fe-B magnets, Journal of applied physics 59(6) (1986) 2244-2246.

[38] W. Mo, L. Zhang, Q. Liu, A. Shan, J. Wu, M. Komuro, Dependence of the crystal structure of the Nd-rich phase on oxygen content in an Nd-Fe-B sintered magnet, Scripta Materialia 59(2) (2008) 179-182.
[40] H. Samata, N. Fujiwara, Y. Nagata, T. Uchida, M. Der Lan, Magnetic anisotropy and magnetostriction of $SmFe_2$ crystal, Journal of Magnetism and Magnetic materials 195(2) (1999) 376-383.
[41] H. Samata, N. Fujiwara, Y. Nagata, T. Uchida, M. Der Lan, Crystal growth and magnetic properties of $SmFe_2$, Japanese journal of applied physics 37(10R) (1998) 5544.
[42] N. Kawamura, T. Taniguchi, S. Mizusaki, Y. Nagata, T. Ozawa, H. Samata, Functional intermetallic compounds in the samarium-iron system, Science and Technology of Advanced Materials 7(1) (2006) 46.
[43] X. Tang, H. Sepehri-Amin, T. Ohkubo, M. Yano, M. Ito, A. Kato, N. Sakuma, T. Shoji, T. Schrefl, K. Hono, Coercivity enhancement of hot-deformed Ce-Fe-B magnets by grain boundary infiltration of Nd-Cu eutectic alloy, Acta Materialia 144 (2018) 884-895.
[44] S. Sugimoto, T. Shimono, H. Nakamura, T. Kagotani, M. Okada, M. Homma, Phase relation of Sm-Fe-V alloys around the compound $Sm_3(Fe,V)_{29}$, Materials transactions, JIM 37(3) (1996) 494-498.
[45] A. Gabay, C. Han, C. Ni, G.C. Hadjipanayis, Phase equilibria in iron-rich Sm-Fe-Ti and Sm-(Fe,Co)-Ti alloys at 1100–1200° C, Journal of Alloys and Compounds 965 (2023) 171444.
[46] H. Okamoto, Cu-Sm (copper-samarium), Journal of phase equilibria 19(2) (1998) 183-183.

Supplementary materials

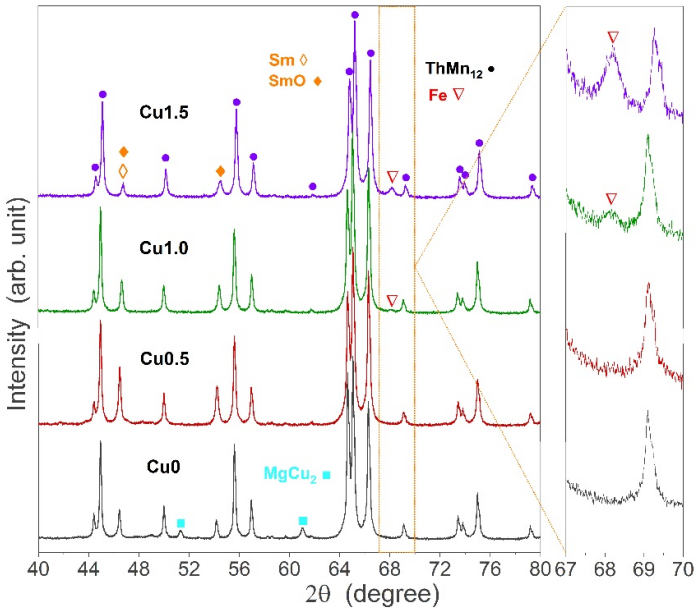

Fig. S1. XRD profiles of $Sm_8Fe_{77-x}Ti_5V_8Al_2Cu_x$ (x=0, 0.5, 1.0, 1.5) magnets after sintering at 1100 ºC for 1.5 h and post-sinter annealing at 1100 ºC for 1.5 h. XRD was conducted on sintered magnets after pulverization to powder.

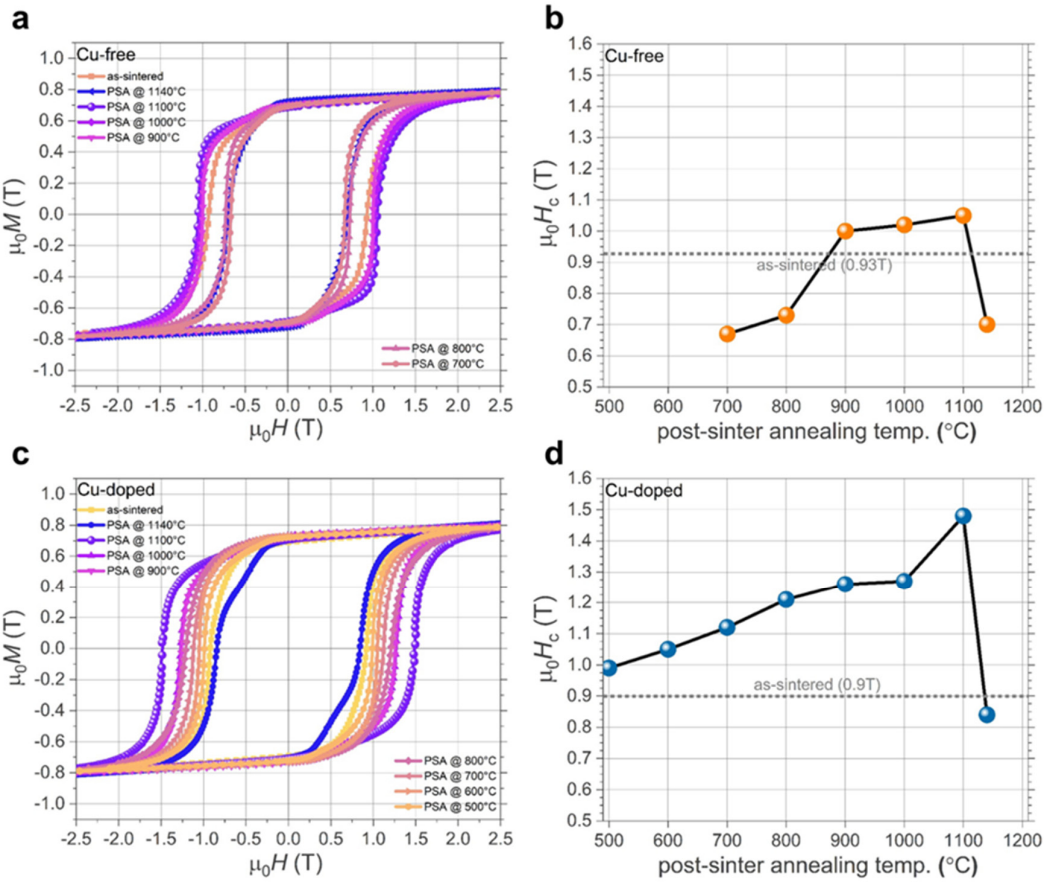

Fig. S2. a), c) Hysteresis loops of as-sintered and post-sinter annealed $Sm_8Fe_{77}Ti_5V_8Al_2$ (Cu-free) and $Sm_8Fe_{76.5}Ti_5V_8Al_2Cu_{0.5}$ (Cu-doped) magnets. b), d) Post-sinter annealing temperature dependent of coercivity $\mu_0 H_c$ for Cu-free and Cu-doped magnets.

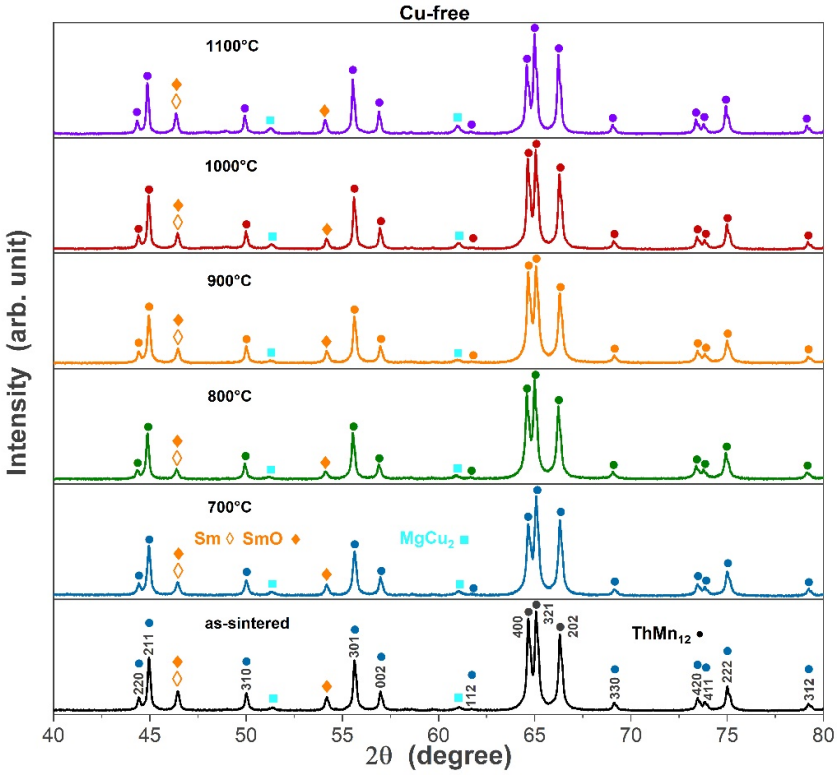

Fig. S3. XRD profiles of as-sintered and post-sinter annealed Cu-free magnets.

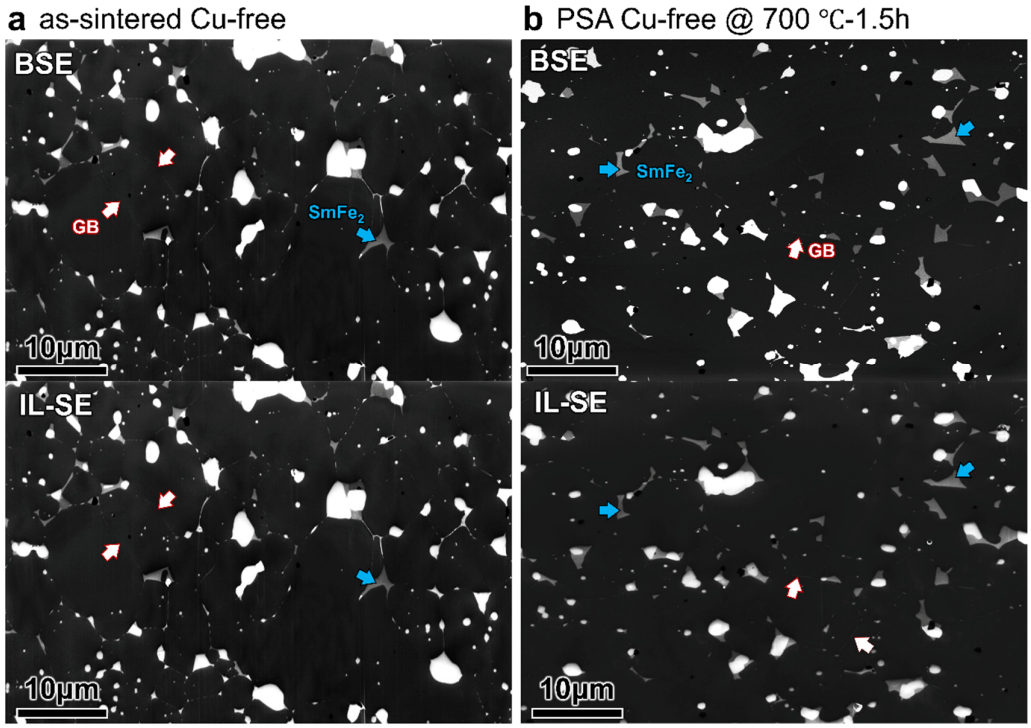

Fig. S4. Backscattered electron (BSE) and In-Lens secondary electron (IL-SE) SEM images

of the Cu-free magnets at as sintered state and after post-sintered annealing at 700 ℃ for 1.5 h.

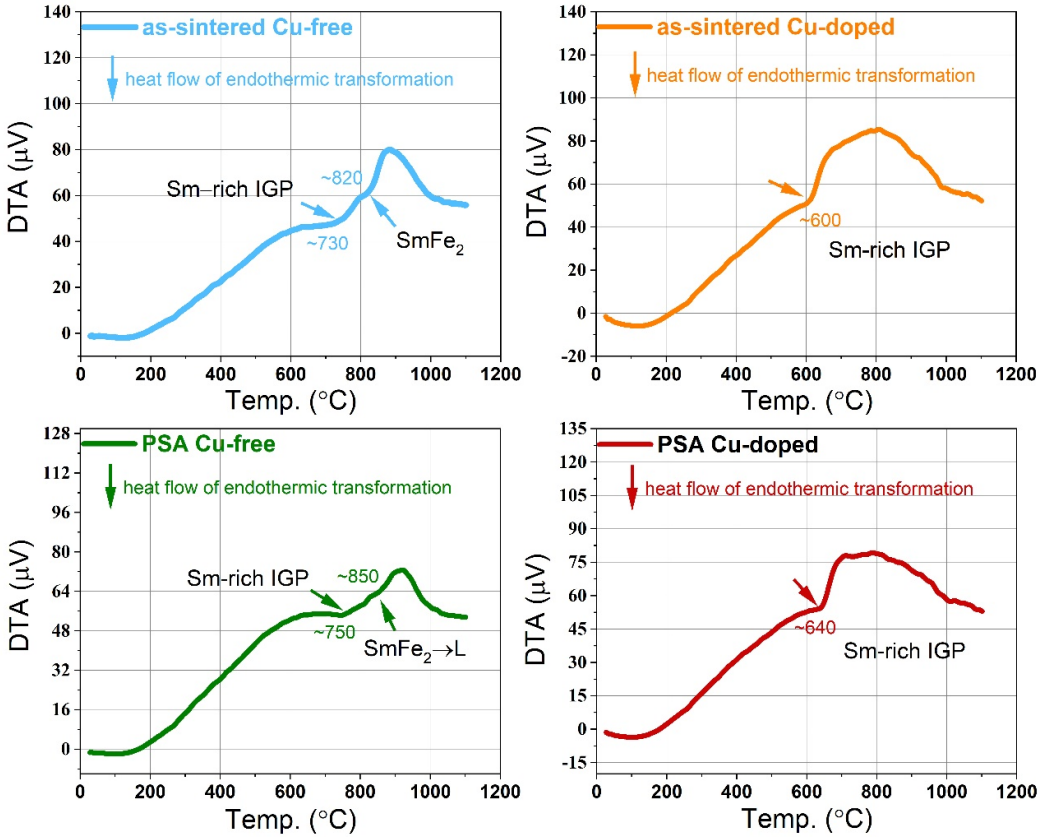

Fig. S5. Differential Thermal Analysis (DTA) curves indicating phase transformation temperature for Cu-free and Cu-doped magnets at as sintered status and optimal post-sinter annealed status.